ChemCatChem

The European Society Journal for Catalysis

Chemistry Europe

European Chemical Societies Publishing

Supported by

GeCatS GERMAN CATALYSIS SOCIETY

Accepted Article

This manuscript has been accepted after peer review and appears as an Accepted Article online prior to editing, proofing, and formal publication of the final Version of Record (VoR). This work is currently citable by using the Digital Object Identifier (DOI) given below. The VoR will be published online in Early View as soon as possible and may be different to this Accepted Article as a result of editing. Readers should obtain the VoR from the journal website shown below when it is published to ensure accuracy of information. The authors are responsible for the content of this Accepted Article.

WILEY-VCH

FULL PAPER

Phyllosilicate-derived nickel-cobalt bimetallic nanoparticles for the catalytic hydrogenation of imines, oximes and N-heteroarenes

Carmen Ciotonea,*,[a,d] Nisrine Hammi,[a,b] Jérémy Dhainaut,[a] Maya Marinova,[d] Adrian Ungureanu,[c] Abdelkrim El Kadib,[b] Christophe Michon,[a,e] and Sébastien Royer*,[a]

Abstract: The development of cost-effective, noble metal-free catalytic systems for the hydrogenation of unsaturated aliphatic, aromatic, and heterocyclic compounds is fundamental for future valorisation of general feedstock. With this aim, we report here the preparation of highly dispersed bimetallic Ni/Co nanoparticles (NPs), by a one-pot deposition-precipitation of Ni and Co phases onto mesoporous SBA-15 silica. By adjusting the chemical composition in the starting mixture, three supported catalysts with different Ni to Co weight ratios were obtained, which were further subjected to treatments under reducing conditions at high temperatures. Characterization of the resulting solids evidenced a homogenous distribution of Ni and Co elements forming the NPs, the best results being obtained for Ni/Co-2:2 samples, for which 50 wt.% Ni – 50 wt.% Co NPs are found located on the surface of the residual phyllosilicate. Ni/Co-2:2, presenting the best performances for the hydrogenation of 2-methyl-quinoline, was further evaluated in the catalytic hydrogenation of selected imines, oximes and N-heretoarenes. Due to the high dispersion of bimetallic Ni-Co NPs, excellent properties (activity and selectivity) in the conversion of the selected substrate are reported.

Introduction

[a] Dr. C. Ciotonea, N. Hammi, Dr. J. Dhainaut, Dr. C. Michon and Prof. S. Royer.
Univ. Lille, CNRS, Centrale Lille, Univ. Artois, UMR 8181 - UCCS - Unité de Catalyse et Chimie du Solide, F-59000 Lille, France. Corresponding author: carmen.ciotonea@univ-lille.fr, sebastien.royer@univ-lille.fr; https://twitter.com/UCCS_8181
[b] N. Hammi and Prof. A. El Kadib
Department Euromed Research Center, Engineering Division, Euro-Med University of Fes (UEMF), Route de Meknes, Rond-point de Bensouda, 30070, Fès, Morocco.
[c] Prof. A. Ungureanu
"Gheorghe Asachi" Technical University of Iasi, Faculty of Chemical Engineering and Environmental Protection, 73 D. Mangeron Bvd., 700050 Iasi, Romania.
[d] Dr. M. Marinova
Univ. Lille, CNRS, INRA, Centrale Lille, Univ. Artois, FR 2638 - IMEC - Institut Michel-Eugène Chevreul, F-59000 Lille, France.
[e] Dr. C.Michon, new address:
Université de Strasbourg, Université de Haute-Alsace, Ecole Européenne de Chimie, Polymères et Matériaux, CNRS, LIMA, UMR 7042, 25 rue Becquerel, 67087 Strasbourg, France.

Supporting information for this article is given via a link at the end of the document.

Hydrogenation of aliphatic, aromatic, and heterocyclic compounds is a major industrial process, often encountered in fine chemistry, energy production and refining. Total hydrogenation is usually conducted at high temperatures, and under hydrogen pressures, while selective hydrogenation toward products of added value is typically obtained in milder conditions and using a selective catalyst.[1] Albeit heterogeneous catalysts are less active than their homogeneous counterparts, they present the advantages of being easily separable from liquid reaction media and of high recyclability, therefore they are predominantly attractive for large scale applications. In particular, catalysts presenting highly dispersed noble metal nanoparticles (Pd, Pt, Ru, Rh, Ir) supported on a porous oxide support, such as silica or alumina, are extensively used in selective hydrogenation reactions. For example, selective hydrogenation of D-glucose into D-sorbitol has been performed in the presence of Ru/HY zeolite.[2] Although highly active and/or selective at relatively low temperature, the scarcity and high cost of noble metals drive the research of alternatives based on abundant transition metals (TMs) such as cobalt, nickel and copper, under monometallic or bimetallic forms.[3e,f] However, the preparation of highly dispersed TM oxide nanoparticles (NPs) supported on oxidic supports remains challenging since a limited thermal stability is usually reported.[3] One solution to circumvent such drawback is to limit NPs reorganization and sintering during the thermal activation steps,[4] as encountered in the case of hydrogenation catalysts.

By far, the most used methods for the preparation of supported catalysts is the impregnation. However, despite the low cost and simplicity of the process, this method has some drawbacks, including the poor dispersion of active elements and the limited metal loading.[4c] Dispersion of metallic active phases has previously been possible through stabilization within layers of mono and bimetallic phyllosilicates. This strategy has commonly been achieved by hydrothermal treatment realized in basic media, usually by using sodium silicate and metal precursors under a high temperature treatment, and such bimetallic materials were successfully applied for reforming reactions.[5a-f] Geus *et al.* first proposed the deposition-precipitation (DP) method, to produce metallic NPs on silica - based support.[5g-i,] In this method, the silica and the metal salts are first mixed in acidic conditions below the isoelectric point of the silica (IEP, pH = 2). The pH is then adjusted toward slightly basic conditions, typically following urea hydrolysis, thus slowly moving the net charge of the silica away from its IEP.[5g] As the silica surface becomes negatively charged, metal ions interact

FULL PAPER

electrostatically with the surface, leading to the formation of a metallic layer, in contact with the SiO_2 surface.[6a] By further increasing the pH of the solution, the silica starts dissolving and a phyllosilicate phase can be formed in the presence of TM. The formation of a phyllosilicate phase is critical to efficiently stabilize TMs NPs.[7] Therefore, the choice of the type of silica support is crucial, as higher surface areas will allow to obtain phyllosilicates of lower particle size, resulting *in fine* in high dispersion of TM NPs.[6b]

Burattin *et al.* first suggested a competitive mechanism for the formation of Ni-phyllosilicate (Ni-PS) governed by the kinetics of silica dissolution which depend on the silica specific surface area, the nature of the pH initiator and the reaction time (for deposition-precipitation).[6a, 7e,f, 8] This mechanism highlighted two reactions pathways which can take place simultaneously: a) hetero-condensation/polymerization, favoring the formation of a 1:1 (TO) Ni-PS with general formula $Si_2Ni_3O_5(OH)_4$; and b) olation/polymerization, leading to the precipitation of $Ni(OH)_2$.[6a] This mechanism was further confirmed by Lehmann *et al.* in their work on Ni-PS stabilized on MCM-41.[6b] In the presence of cobalt, the formation of 2:1 (TOT) phyllosilicates, where tetrahedral SiO_4 sheets sandwich a layer of cobalt aqua-complex with the general formula $CoO_x(OH)_{2-x}(Si_2O_5)_2$, is favored.[9] The 2:1 phyllosilicates present higher thermal stability, yet their utilization is limited by the high reduction temperature (> 850 °C) necessary to obtain metallic Co NPs.[11,12] In addition, while the monometallic DP-derived materials are largely used in catalysis,[13] bimetallic counterparts are far less studied due to the different preparation conditions necessary for the controlled precipitation of both metallic precursors.

In this work, we report the preparation of NiCo-derived phyllosilicates by deposition-precipitation initiated by urea. Purely silicic SBA-15 with high specific surface area was used as the support, and different Ni/Co weight ratios were evaluated to form the bimetallic catalysts. Extensive characterization of the materials both in calcined and in their reduced forms was performed to investigate the phyllosilicate properties as well as the final metallic Ni/Co catalyst characteristics. The performance of these supported Ni/Co bimetallic NPs was evaluated for the catalytic hydrogenation of imines, oximes and N-heteroarenes.

Results and Discussion

The textural properties of the calcined Ni/Co-phyllosilicates (Ni/Co-PS) stabilized on SBA-15 were evaluated by nitrogen physisorption at -196 °C. The isotherms and pore size distribution are presented in Figure 1-a) and b), while the related quantitative information are displayed in Table 1.

The parent SBA-15 support exhibited a typical Type IV adsorption-desorption isotherm, with H1 hysteresis having parallel adsorption and desorption branches and a plateau at high P/P_0. Such characteristics confirmed the presence of narrow distribution of the cylindrical pores.[14] As already reported for monometallic DP-derived materials, all Ni/Co-PS presented isotherms of Type IV with H3 hysteresis. This behavior suggested the presence of slit-shaped pores with a broader pore size distribution as illustrated in Figure 1-b).[12]

Such evolution showed a lower long-range ordering of pore structure in the Ni/Co-PS materials, along with the formation of larger cavities (up to 25 nm) by comparison with the initial pore size of the diameter SBA-15 (average size of 6.9 nm).
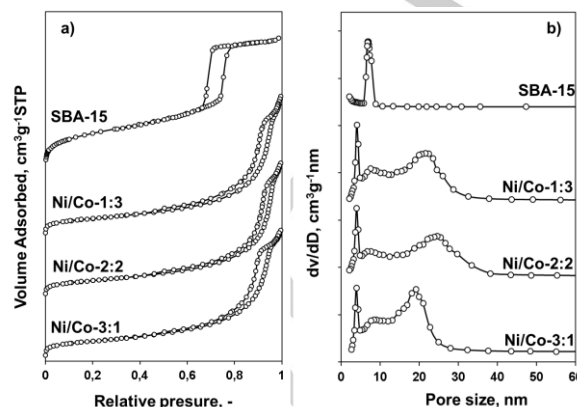

Figure 1. Nitrogen adsorption/desorption isotherms (a) and pore size distribution; (b) obtained for the parent SBA-15 and for calcined Ni/Co-PS materials.

Table 1. Textural properties for the calcined Ni/Co-PS and for the parent SBA-15.

Sample	S_{BET}[a] $m^2.g^{-1}$	S_μ[b] $m^2.g^{-1}$	V_p[c] $cm^3.g^{-1}$	V_μ[d] $cm^3.g^{-1}$	D_{pore}[e] (nm)
SBA-15	780	199	1.16	0.06	6.9
Ni/Co-1:3	323	104	1.06	0.02	3.9-23
Ni/Co-2:2	316	73	1.02	0.017	3.9-25
Ni/Co-3:1	332	121	0.98	0.029	3.9-19

[a] BET surface area; [b], micropore surface area; [c] total pore volume; [d] micropore volume; [e] BJH pore diameter calculated on desorption branch.

Under the synthesis conditions, the SBA-15 framework was partially degraded due to the dissolution of silica in alkaline conditions.[12,15] As observed in Table 1, this dissolution process, necessary for the formation of the phyllosilicate phases, affected the total specific surface area, which decreased by about 60% compared with SBA-15, while the pore volume was less affected by the dissolution-reprecipitation process (a decrease by ~20%). The formation of a new population of pores of 3.9 nm diameter (Figure 1-b), related to the presence of phyllosilicate phases,[16] was observed.

TEM was used to observe the morphological characteristics of the calcined Ni/Co-PS materials and representative images are illustrated in Figure 2. Besides SBA-15 grains presenting ordered mesopores, DP-derived materials showed the presence of filaments which confirmed the formation of phyllosilicates.[17] Small filamentous particles could be found inside the SBA-15 grains (Fig. 2.a-c), while larger filamentous
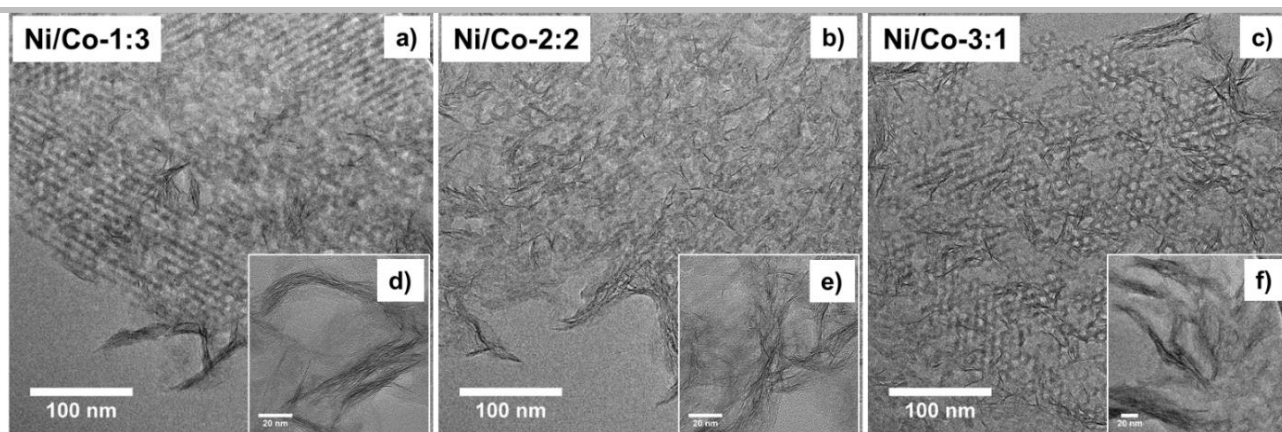
FULL PAPER

Figure 2. Representative TEM images obtained for calcined Ni/Co-PS stabilized on SBA-15. a-c) PS filaments formed inside the SBA-15 porosity. d-f) PS filaments formed on the external surface of the silica grains.

particles were observed at the external surface of the silica grains (Fig. 2.d-f). These results confirmed the partially preserved pore structure after 24 h of DP process. EDX spectra were conducted on all the Ni/Co-PS samples. As expected, the Ni/Co ratios measured by EDX were close to the expected values at ±5 at.% (some examples with Ni/Co values of 73/27 for Ni/Co-1:3; 49/51 for Ni/Co-2:2 and 26/73 for Ni/Co-3:1 are given in Figure S1). A homogeneous composition of the filamentous particles was suggested by EDX analysis, performed on filaments situated inside the SBA-15 grains and on free external filaments. From the TEM images, no clear information about the type of phyllosilicate synthesized (1:1 or 2:1) could be obtained.

The overall view on the materials did not reveal the presence of any individual NiO or Co_3O_4 bulky particles as usually obtained using classical (wet or incipient wetness) impregnation route, indicating an almost complete incorporation of the metallic precursors within the phyllosilicate layers.
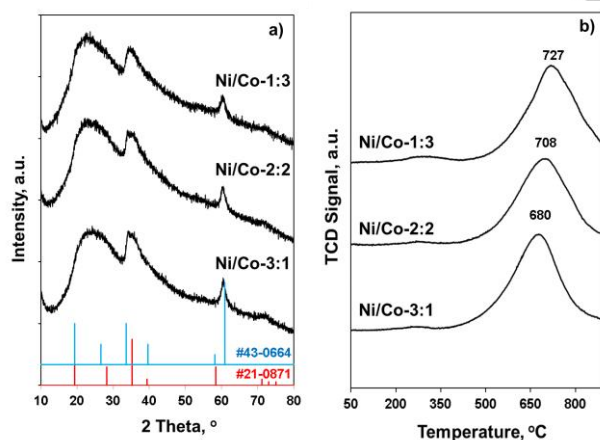

Figure 3. X-ray diffractograms. Bottom: Blue bars are for ICDD reference No 43-0664 (Kerolite phase); Red bars are for ICDD reference No 21-0871 (Smectite phase) (a) and TPR profiles of the calcined Ni/Co-PS based materials (b).

The morphology for the bimetallic PS was indeed similar to the one obtained for the monometallic Ni or Co phyllosilicates.[12] Wide-angle PXRD patterns of Ni/Co-PS are showed in Figure 3-a). Reflections were observed at 33°, 35° and 60°. Their positions fit with nickel 1:1 phyllosilicate (kerolite phase, ICDD reference no 43-0664) and cobalt 2:1 phyllosilicate (smectite phase, ICDD reference no 21-0871). The type of phyllosilicate formed can usually be revealed by the position of the peaks at 33°-35° and 58°-63°. However, here these peaks were asymmetric and too broad to be assigned to a unique phase and did not allow to conclude on the presence of pure Ni-PS 1:1 or Co-PS 2:1 phases.

Still, the presence of the reflections as well as the aspect of materials as observed in TEM images, i.e. the presence of filamentous particles, were clear evidence of the phyllosilicate phases whatever the Ni to Co weight ratio.

The reducibility of Ni/Co-PS was evaluated by using temperature programmed reduction under H_2 flow (TPR), and the profiles obtained are represented in Figure 3-b). An almost complete reduction of the metals was calculated from the total hydrogen consumption during the TPR experiments, with values of reduction of M(+III) or M(+II) to M(0) comprised in the 93-96 at.% range (Table 2). Such high values indicated that most of the metallic NPs, were accessible to the gas phase. However, the high temperature characterized the stabilization effect of the phyllosilicate phase. Interestingly, the temperature of maximum hydrogen consumption (T_{max}) values decreased from 727 °C to 680 °C, while increasing the nickel content in the material. A similar trend was observed previously by Bian and Kawi for materials based on 10 wt.% Ni-Co deposed on colloidal silica. Authors reported reduction temperatures comprised between 700 and 800 °C, and increasing with the Co content in the materials to reach the maximum reduction temperature of 800 °C for pure Co phyllosilicate.[18] These T_{max} are comprised between the reduction temperature of pure Ni-PS, reported at around 630 °C [19], and the reduction temperature of pure Co-PS reported at 800 °C. [11,12,20] Accordingly, the presence of nickel, which even at a low weight content (5 wt.% in Ni/Co-1:3) orientates the formation of a 1:1 (T:O) phyllosilicate phase at the expense of the 2:1 (T:O:T)

FULL PAPER

phyllosilicate phase, or the reduction of nickel at lower temperature could allow the reduction of cobalt 2:1 PS phase at significantly lower temperature than encountered for pure Co 2:1 phyllosilicate.

PXRD analysis was performed over Ni/Co-PS materials, after reduction at 700 °C (Figure S2). Complete reduction of the phyllosilicate phase was confirmed. For the three materials, the patterns are displaying reflections at similar 2θ angles (43°, 51° and 75°), which were assigned to the (111), (200) and (220) planes. By comparison with Ni^0 having reflections at 2θ = 44°, 51° and 76° (ICDD reference No. 04-0850) and Co^0 having reflections at 2θ = 41°, 44°, 47° and 75° (ICDD reference No. 05-0727), we can assign the new reflections to the formation of Ni-Co alloys[21] or individual metallic NPs. Using Scherrer equation, average crystal domain sizes are calculated at 7 nm for Ni/Co-1:3, 6.6 nm for Ni/Co-2:2 and 9.4 nm for Ni/Co-3:1. This supports the stabilization effect of the NPs by the PS phase. The localization and size homogeneity

Table 2. Reduction characteristic of the calcined Ni/Co-PS stabilized on SBA-15.

Sample	T_{max}, °C	H_2 consump.[a] mmol.g^{-1}	Ni-Co red. Degree[b], %
Ni/Co-1:3	680	3.24	95
Ni/Co-2:2	708	3.27	96
Ni/Co-3:1	727	3.22	93

[a] Total hydrogen consumption at the issue of the TPR experiment; [b] reduction degree calculated on the basis of the reduction of divalent metal to zero valent metal ($Ni^{2+} \rightarrow Ni^0$; $Co^{3+} \rightarrow Co^{2+} \rightarrow Co^0$).

of the metallic Ni/Co NPs onto the silica support were evaluated by HAADF imaging, after exposure to a reductive atmosphere same conditions as for the activation of the catalyst before the catalytic test.
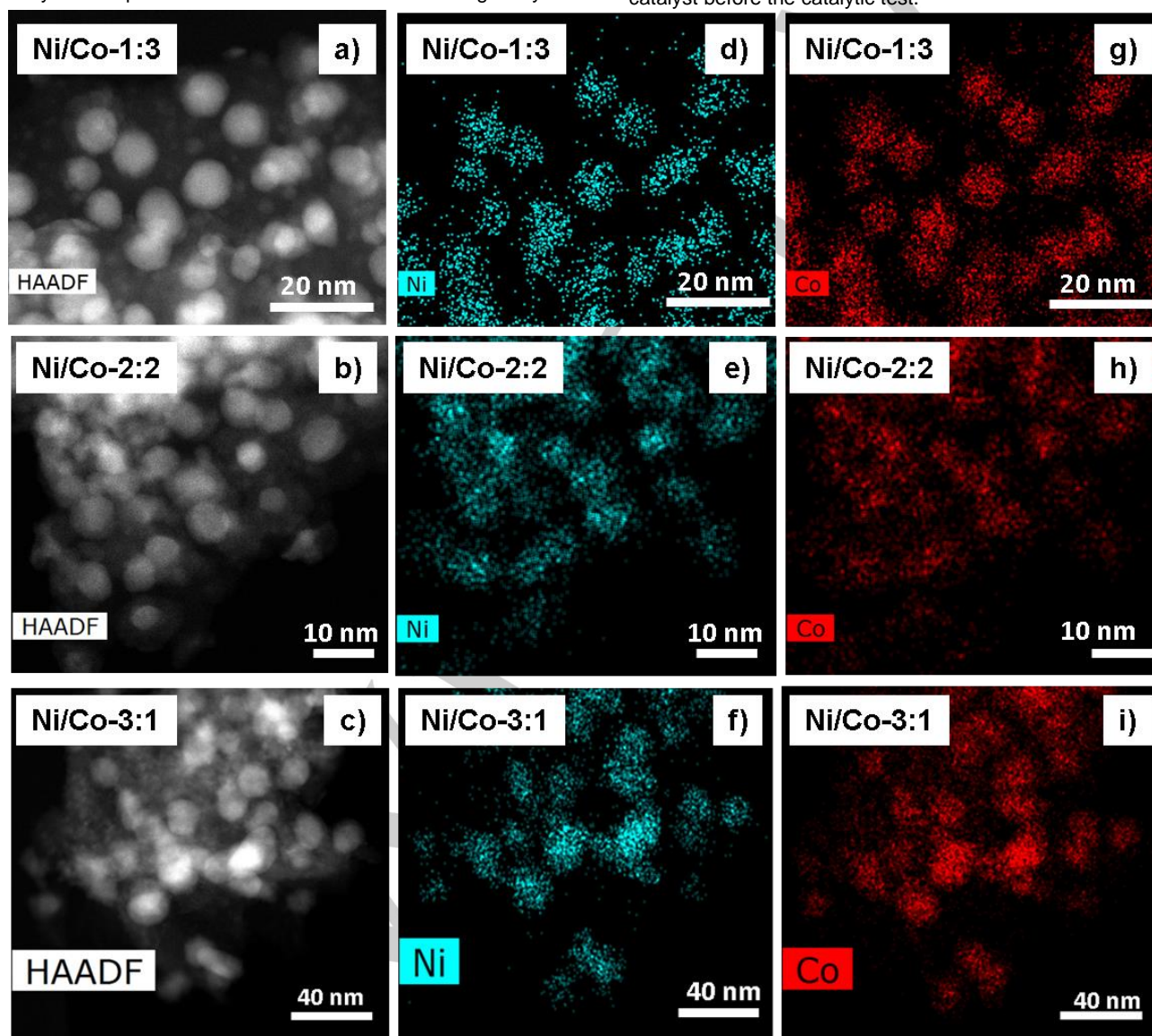

Figure 4 (a,b,c) Representative HAADF images obtained for Ni/Co-PS after reduction at 700 °C; (d,e,f) nickel localization as determined by STEM-EDX mapping analysis; (g,h,i) cobalt localization as determined by STEM-EDX mapping analysis.

FULL PAPER

Table 3. Performance of the different reduced Ni/Co-PS catalysts for the hydrogenation of N-heterocycles.

Entry	Reagent	Product	Time (h)	Yield (%)[a],[b]
1	**1a**	**2a**	13	71
2	**1b**	**2b**	13	50
3	**1c**	**2c**	13	94
4	**1d**	**2d**	13	96
5	**1e**	**2e**	13	99
6	**1f**	**2f**	13 / 48	17 / 41
7	**1g**	**2g**	88	47[c]
8	**1h**	**2h**	88	12[c]
9	**1i**	**2i**	13 / 61	36 / 99
10	**1j**	**2b**	13	54
11	**1k**	None - No reaction	13	0
12	**1l**	**2l**	13	94

[a] Reaction conditions: 0.7 mmol of reactant; catalyst, 0.005 g, isopropanol 4.0 mL; H_2 (50 bar); 80 °C. [b] Determined by GC

[c] Reaction performed in the presence of 1 equivalent of (R)-(-)-Camphor-10-sulfonic acid. No reaction without.

Representative images are illustrated in Figure 4, with additional STEM-EDX mapping performed at high magnification in order to evaluate the degree of homogeneity of the produced NPs. STEM-EELS elemental analyses were also performed on selected areas and are shown in Figure S3. The histograms corresponding to the reduced samples are presented in Figure S4. After reduction at 700 °C, Ni/Co NPs were observed, without any residual filament of PS, an observation in agreement with the almost complete reduction of the transition metal cations when activated at 700 °C under H_2 flow (TPR and XRD analyses). The images presented in Figure 4-a) d) g), Figure S3 and Figure S4, illustrated the results obtained for the Co-rich sample (Ni/Co-1:3). The sample Ni/Co-1:3 presents two population of particles: i) small (>1 to 4 nm) with a majority of 1 nm sized particles and fewer of 2 nm size; ii) large (5 to 9 nm) with a majority of 5 and 6 nm sized particles and fewer of 7 and 8 nm size. The element mapping, presented in Figure 4 and Figure S3, showed that the small particles are mostly composed of Co while the larger particles are composed of both Ni and Co. Both STEM-EDX and STEM-EELS analyses revealed uniform distribution of Ni at 20±5 at.% and Co at 80±5 at.% for all observed NPs, the presence of both elements in the larger NPs being evidenced in Figure 4 d) and g). Of note, the smaller NPs were significantly enriched in Co (80±5 at.%). In the case of

FULL PAPER

Ni/Co-2:2, a uniform distribution of the NPs size was observed, with particles between 1 to 6 nm (Figure S4), and an element mapping showing the presence of both Ni and Co in the particles. The STEM-EDX and STEM-EELS analyses showed a global uniform composition of the 7 nm NPs in Ni (50±5 at.%) and Co (50±5 at.%). From STEM-EELS analysis (Figure S3-Ni/Co-2:2), it appeared that the shell of these nanoparticles is enriched in Co (around 85 at.%) while the core enriched in Ni (around 70 at.%). The particles of low size, <3 nm, remain significantly enriched in Co. Finally, the Ni/Co-3:1 sample presents a broad distribution of particles sizes by comparison to the previous two materials (Figure S4). Though a small proportion of low size NPs (<2 nm) is observed, most of the particles were larger with sizes observed to be located between 3 and 6 nm, with a non-negligible proportion of particle of size above 10 nm. This clearly demonstrated a depressed degree of dispersion in this material. STEM-EDX mapping evidenced the presence of both elements in all observed NPs, with a composition fitting with the awaited one (65±5 at.% in Ni and 35±5 at.% in Co).

The catalytic properties of the three materials were then evaluated by studying the hydrogenation of 2-methyl-quinoline **1a** (Table S1). Among the mixed metal catalysts, Ni/Co-1:3 and Ni/Co-3:1 materials exhibited activities of 46 % and 67 %, whereas the highest activity of 71 % was obtained for Ni/Co-2:2. If we compare the bimetallic catalysts with the monometallic counterparts (Table S2- catalytic test for 1b substrate), Ni monometallic catalyst presents the highest activity (56 %, under the conditions selected), that is not surprising since Ni phase is reported as highly active, and activity is related to the 111 plane exposed.[22] Co-catalyst presents significantly lower activity (35%, Table S2), while Ni/Co-2:2 presents activity slightly below than that of the pure nickel catalyst despite a two times lower Ni content. The formation of well-dispersed Ni-Co mixed NPs [23], stabilized onto the silica surface, was however expected to show improved catalyst stabilities in the hydrogenation of selected substrates.[24]

The reduced Ni/Co-2:2 was selected as a model catalyst in the hydrogenation of various N-heterocycles, imines and oximes (Tables 3 and 4). At first, the hydrogenation of 2-methyl-quinoline **1a** and quinoline **1b** proceeded well in 13 hours at 80 °C and 50 bar of hydrogen gas affording the reduced products in good to average yields (Table 3, entries 1 and 2). While the reductions of acridine **1c**, pyridine **1d** and pyrazine **1e** were achieved in almost quantitative yields within 13 hours (entries 3-5), the benzo-quinoline **1f** needed 48 hours to reach an average yield (entry 6). The hydrogenation of 2-Methyl-indole **1g** and indole **1h** was even harder, requiring 88 hours of reaction time and the use of a stoechiometric amount of (*R*)-(-)-Camphor-10-sulfonic acid in order to proceed.[25] The corresponding reduced products **2g** and **2h** were respectively obtained in average to low yields (entries 7 and 8). Regarding functionalized quinolines, the hydrogenation of 8-hydroxyquinoline **1i** was almost quantitative within 61 hours (entry 9). However, the reaction of 2-chloro-quinoline **1j** led exclusively to the dechlorinated product **2b** (entry 10) and the nitrile function of substrate **1k** prevented the hydrogenation (entry 11). Finally, the reaction of quinoline **1l** resulted in the product **2l** through simultaneous reduction of both heterocycle and aldehyde function (entry 12).
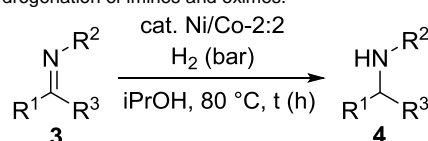
Afterwards, the bimetallic Ni/Co-2:2 NPs material was successfully used to catalyse the hydrogenation of various imines and oximes (Table 4). Under a hydrogen gas pressure of 10 bar, ketimines **3a-d** bearing aromatic and/or aliphatic substituents were all hydrogenated quantitatively (entries 1-4) within 13 hours at 80 °C. By comparison, the hydrogenation of oximes **3e-g** required a higher hydrogen pressure (20 bar) and 36 hours of reaction in order to proceed in high yields (entries 5-7).

Finally, the recycling of the bimetallic reduced Ni/Co-2:2 material was investigated by studying the hydrogenation of 2-methyl-quinoline **1a** (see supplementary file Table S3). Due to the sensitivity of the catalyst, the recycling process was performed under the strict exclusion of air. Although the catalyst was reused up to 5 cycles, we noticed a significant loss of activity at each cycle, the yield decreasing gradually from 72 % at cycle 1 to 21 % at cycle 5.
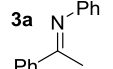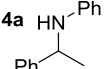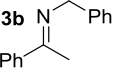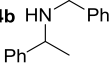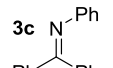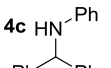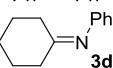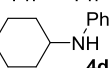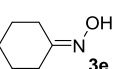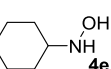
In order to inform on the state of the spent catalyst, the materials after the catalytic tests on substrates 1a and 1d were analyzed by HAADF-TEM-coupled with EDX analysis (Figure S5). The corresponding metallic particle size histograms are displayed in Figure S6. After the hydrogenation of **1a** and **1d** substrates and even after 5 recycling cycles for **1a** hydrogenation (Table S3), the particles presented limited sintering. Only 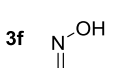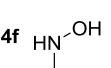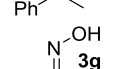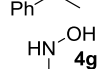the smallest size population (< 2 nm) is affected and is observed to increase by 1-2 nm, while the maximum size is always observed around 8 nm (Figures S5 and S6). By observing the TEM images, there was no visible evidence of consequent coke accumulation around the catalyst (like carbon filament formation). These results confirmed a better stability of the bimetallic Ni/Co-2:2 based material as compared to the monometallic catalyst along the hydrogenation reactions (Table S2). The alloying approach described herein seems to prevent the formation of carbonaceous species such as nickel carbide, which easily forms in Ni/SiO$_2$ materials.[26] However, even if the recycling tests were performed under the strict exclusion of air, a surface reoxidation (mostly on the Co atoms[18]) could not be completely excluded, which can contribute to the catalyst deactivation in addition to the poisoning of active sites by organics.

To the best of our knowledge, though applications in the hydrogenation of nitrobenzene, phenols and conjugated carbonyl compounds have been reported,[23a,27a-c] bimetallic Ni-Co nanoparticles have never been applied in the hydrogenation of imines, oximes and quinolines. However, Ni-Co nanoparticles supported on SiO$_2$ support using heteronuclear metal-organic frameworks (MOFs) as metal alloy precursors were successfully applied in the hydrogenation of furfuryl alcohol.[27d] Such catalytic reaction was carried out at a similar temperature (80 °C) but with a lower hydrogen pressure (30 bar) and shorter reaction time (8 versus 13 hours) compared to the catalytic parameters selected to be used in this work. Under the conditions applied for furfuryl alcohol, the catalyst maintained high conversions and selectivities along five consecutive runs keeping its crystal structure homogeneity and similar nanoparticles size.

Table 4. Hydrogenation of imines and oximes.

$$R^1 \underset{R^3}{\overset{N-R^2}{=}} \quad \xrightarrow[\text{iPrOH, 80 °C, t (h)}]{\overset{\text{cat. Ni/Co-2:2}}{\underset{H_2 \text{ (bar)}}{}}} \quad R^1 \underset{R^3}{\overset{HN-R^2}{\diagup}}$$

3 → 4

FULL PAPER

Entry	Reagent 3	Product 4	t (h)	H$_2$ (bar)	Yield[a, b] (%)
1	3a (N–Ph, Ph, Ph)	4a (HN–Ph, Ph, Ph)	13	10	>99
2	3b (N–Ph, Ph)	4b (HN–Ph, Ph)	13	10	>99
3	3c (N–Ph, Ph, Ph)	4c (HN–Ph, Ph, Ph)	13	10	>99
4	3d (cyclohexyl N–Ph)	4d (cyclohexyl NH–Ph)	13	10	>99
5	3e (cyclohexyl N–OH)	4e (cyclohexyl NH–OH)	36	20	>99
6	3f (N–OH, Ph)	4f (HN–OH, Ph)	36	20	>99
7	3g (N–OH, Ph, Ph)	4g (HN–OH, Ph, Ph)	36	20	96

[a] Reaction conditions: 0.7 mmol of reactant; catalyst (0.005 g); isopropanol 4.0 mL; H$_2$ (bar); 80 °C, 13 h; [b] Yield measured by ^{1}H NMR.

Conclusions

To summarize, bimetallic Ni/Co phyllosilicates stabilized on SBA-15 were prepared at three Ni/Co ratios (3:1, 2:2, and 1:3) using deposition-precipitation in the presence of urea as precipitation initiator. The materials were characterized in their calcined form by N$_2$ physisorption, high resolution STEM-EDX, and PXRD. All Ni/Co-PS materials displayed high specific surface, and a homogenous distribution of the Ni and Co cations within the phyllosilicate phase. After high temperature reducing treatment, no more phyllosilicate phase was observed, leading to the formation of highly dispersed Ni/Co bimetallic NPs as observed by HAADF imaging-EDX and STEM-EELS. The bimetallic precursors presented lower reduction temperatures (680 - 727 °C depending on the Ni/Co ratio) compared to the temperature needed for the reduction of pure monometallic Co (> 850 °C), which shows a synergy between the two metal during reduction step. The best results were obtained for the Co/Ni ratio of 1 in the catalyst. In this last case, a homogenous distribution of Ni and Co elements was evidenced by STEM-EELS and STEM-EDX analyses in the bimetallic nanoparticles, together with a high degree of dispersion (size of observed particle exclusively below 9 nm). After pre-screening, the latter catalyst was selected for catalytic hydrogenation. This transition metals-based catalyst allowed the hydrogenation of several N-heterocycles, imines and oximes, with both high activities and selectivities being obtained for a range of substrates. Catalyst activity decreased upon recycling, and suggested that an intermediate treatment for reactivation was needed between each cycle. Further studies are ongoing in our laboratory to understand the origin of the catalysts deactivation and for enhancing their stability.

Experimental Section

Sample synthesis

Support: SBA-15 support was synthesized according to the procedure proposed by Zhao et al.[14] In a typical procedure, 4.00 g of Pluronic P123 was added to 150 mL of HCl solution (1.6 M), and the solution was stirred at 40 °C for 6 h. Then the silica source, 8.5 g of TEOS was added dropwise to the solution and the stirring was maintained for 24 h. The resulting white suspension was submitted to a hydrothermal treatment at 100 °C for 48 h. The solid was thereafter collected by filtration, washed with distilled water, and dried at 80 °C for 12 h. The porous SBA-15 support was obtained by calcination at 550 °C for 6 h in a muffle oven (heating ramp 1.5 °C min^{-1}). The sample is denoted SBA-15.

Deposition precipitation method: The nickel and cobalt incorporation in the silica support was performed using Deposition-Precipitation (DP) route. A suspension containing 1.6 g of calcined SBA-15 support and an aqueous solution of nickel and cobalt nitrate was prepared. The composition of solution was adjusted to reach the desired Ni and Co metal loading of 20 wt.%, with three different ratio of Ni to Co of 1:3, 2:2 and 3:1 respectively. The solution was placed in a double wall thermostated reactor, at a temperature of 90 °C. The pH of the suspension was adjusted to 2.0, by adding nitric acid drops, and then urea solution (3 mol L^{-1}) was added dropwise. To ensure a complete precipitation, the solution was stirred for 24 h at 90 °C under reflux. At the end of the reaction, the pH obtained was 7.4±0.1. pH evolution with time was monitored during all the precipitation step. The obtained solid was collected by filtration, followed by washing with distilled water and drying at 40 °C for 12 h. Finally, the material was calcined at 500 °C for 6 h (heating ramp 1.5 °C min -1).[12] Materials prepared by DP are denoted in the text Ni/Co-x:y (where x:y is the Ni to Co ratio 1:3; 2:2 and 3:1).

Characterization procedure

N$_2$-physisorption isotherms were recorded at -196 °C on a Micromeritics Tristar II automated gas sorption system. Before analysis, the samples were outgassed under dynamic vacuum at 350 °C for 3 h. Textural properties were calculated from the adsorption/desorption isotherms by using Tristar II software version 1.55. Specific surface area was determined using the multipoint B.E.T. algorithm in the P/P$_0$ range from 0.10 to 0.25. The mesopore size distribution was determined by BJH equation on desorption branch. Pore volume was determined at P/P$_0$ = 0.98, on the adsorption branch.

Powder X-ray diffraction (PXRD) was performed on the powder samples, using a Bruker X-ray AXS D8 Advance diffractometer in Bragg-Brentano geometry configuration fitted with a LynxEye Super Speed detector. XRD patterns were recorded with Cu Kα radiation (λ = 0.154 nm, 40 kV, 30 mA) in the 10–80° 2θ range with a 0.02° 2θ step. Phase identification was made by comparison with the ICDD database.

Micrographs (transmission electron microscopy, TEM) on oxidized samples were recorded on a JEOL 2100 UHR instrument (operated at 200 kV with a LaB$_6$ source and equipped with a Gatan Ultra scan camera), with a resolution of 0.19 nm, and equipped with an Energy Dispersive X-ray Spectroscopy (EDXS) detector. All the samples were embedded in a polymeric Epoxy resin (spurr) and cut into sections of 50 nm using an ultramicrotome equipped with a diamond knife. Cuts were deposited on carbon grids for analysis. The images on samples reduced at 700 °C were collected on a TITAN Themis 300 S/TEM with a probe aberration corrector and monochromator, allowing spatial resolution of 65 pm and energy resolution of 150 meV. The microscope was equipped with a super-X windowless 4 quadrant SDD (silicon drift detector) detection system for the STEM-EDX mapping and with several annual dark field detectors and a Quantum ERS/966 GIF with Dual EELS for simultaneous acquisition of low and high energy losses. The experiment was performed with a 0.5 nm probe size, a convergence angle of 21 mrad and a probe current of approximately 100 pA. For the high angle annular dark field (HAADF), images collection semi-angles have been between 50 and 200 mrad. For the STEM-EELS acquisition the energy resolution has been of about 0.9 eV, the EELS entrance aperture has been 2.5 mm and collection semi-angle of 50 mrad. For the STEM-EELS

FULL PAPER

spectrum images 20 to 50 ms of dwell times have been used with 0.1 nm pixel size.

H_2-TPR was conducted on an Autochem chemisorption analyzer (Micromeritics), equipped with a TCD. Consumed H_2 was driven from the TCD signal after calibration. Before H_2-TPR run, the solid was activated up to its calcination temperature (from room temperature to 500 °C, heating ramp of 10 °C min^{-1}, and isothermal time of 1 h) under simulated air at a total flow rate of 50 mL min^{-1}. After cooling down to 35 °C, the H_2 containing flow was stabilized (50 mL min^{-1}, 5.0 vol.% H_2 in Ar) and the temperature-programmed reduction was performed (from 50 °C to 900 °C, with a temperature ramp of 10 °C min^{-1}).

General Procedures for the catalytic hydrogenations of imines, oximes and N-heterocycles under hydrogen pressure -

Heterocycles

Heterocycle reagent (0.7 mmol, 1 eq.), selected reduced catalyst (0.0050 g) were introduced in an autoclave and dried under vacuum for 10 minutes. Under a nitrogen flow, the dry isopropanol solvent (4 mL) was added. The autoclave was then filled with hydrogen at a pressure of 50 bar after 3 purges. The reaction mixture was then heated at 80 °C under stirring during the selected time (usually 13 hours). At the end of the reaction, autoclave was cooled then degassed. The crude reaction product was recovered after filtration over Celite and solvent evaporation under vacuum. It was then directly purified by flash chromatography.

Imines: Imine reagent (0.7 mmol, 1 eq.), selected reduced catalyst (0.0050 g) were introduced in an autoclave and dried under vacuum for 10 minutes. Under a nitrogen flow, the dry isopropanol solvent (4 mL) was added. The autoclave was then filled with hydrogen at a pressure of 10 bar after 3 purges. The reaction mixture was then heated at 80 °C under stirring during the selected time (usually 13 hours). At the end of the reaction, autoclave was cooled then degassed. The crude reaction product was recovered after filtration over Celite and solvent evaporation under vacuum. It was then directly purified by flash chromatography.

Oximes: Oxime reagent (0.7 mmol, 1 eq.), selected reduced catalyst (0.0050 g) were introduced in an autoclave and dried under vacuum for 10 minutes. Under a nitrogen flow, the dry isopropanol solvent (4 mL) was added. The autoclave was then filled with hydrogen at a pressure of 20 bar after 3 purges. The reaction mixture was then heated at 80 °C under stirring during the selected time (usually 36 hours). At the end of the reaction, autoclave was cooled then degassed. The crude reaction product was recovered after filtration over Celite and solvent evaporation under vacuum. It was then directly purified by flash chromatography.

[1] a) A. J. Marchi, J. L. G. Fierro, J. Santamaría, A. Monzón, *Appl. Catal. A-Gen.* **1996**, *142*, 375- 386; b) P. Mäki-Avela, J. Hájek, T. Salmi, D. Yu. Murzin, *Appl. Catal. A-Gen.* **2005**, *292*, 1-49; c) M. J. Suh, S. K. Ihm, *Top. Catal.* **2010**, *53*, 447-454, d) X. M. Liu, G. Q. Lu, Z. F. Yan, J. Beltramini, *Ind. Eng. Chem. Res.* **2003**, *42*, 6518-6530.

[2] D. K. Mishra, A. A. Dabbawala, J. J. Park, S. H. Jhung, J. -S. Hwang, *Catal. Today,* **2014**, *232*, 99-107.

[3] a) L. Jiao, J. R. Regalbuto, *J. Catal.* **2008**, *260*, 342-350; b) N. Brodie-Linder, R. Besse, F. Audonnet, S. LeCaer, J. Deschamps, M. Impéror-Clerc, A. Simionesco, *Microp. Mesop. Mater.* **2010**, *132*, 518-525; c) P. C. M. van Stiphout, D. E. Stobbe, F. T. V. D. Scheur, J. W. Geus, *Appl. Catal.* **1988**, *40*, 219-246; d) J. R. A. Sietsma, J. D. Meeldijk, J. P. den Breejen, M. Versluijs-Helder, A. J. van Dillen, P. E. de Jongh, K. P. de Jong, *Angew. Chem.* **2007***, 119*, 4641-4633, *Angew. Chem. Int. Ed.* **2007**, *46*, 4547-4549. e) R. M. Bullock, *Science* **2013**, *342*, 1054-1055; f) J. R. Ludwig, C. S. Schindler, *Chem* **2017**, *2*, 313-316.

[4] a) J. R. A. Sietsma, H. Friedrich, A. Broersma, M. Versluijs-Helder, A. J. van Dillen, P. E. de Jongh, K. P. de Jong, *J. Catal.* **2008**, *260*, 227-235; b) H. Friedrich, J. R. A. Sietsma, P. E. de Jongh, A. J. Verkleij, K. P. de Jong, *J. Am. Chem. Soc.* **2007**, *129*, 10249-10254; c) J. R. A. Sietsma, J. D. Meeldijk, M. Versluijs-Helder, A. Broersma, A. J. van Dillen, P. E. de Jongh, K. P. de Jong, *Chem. Mater.* **2008**, *20*, 2921-2931; d) P. de Jong, P.E. de Jongh, *Catal. Today* **2011**, *163*, 27-32.

[5] a) Z. Bian, I. Y. Suryawinata, S. Kawi, *Appl.Catal. B: Environ.* **2016**, *195*, 1-8; b) Z. Bian, Z. Li, J. Ashok, S. Kawi, *Chem. Commun.* **2015**, *51*, 16324-16326; c) J. Ashok, Z. Bian, Z. Wang, S. Kawi, *Catal. Sci. Technol.* **2018**, *8*, 1730-1742; d) S. Das, J. Ashok, Z. Bian, N. Dewangan, M.H. Wai, Y. Du, A. Borgna, K. Hidajat, S. Kawi, Appl. Catal.B: Environ. **2018**, *230*, 220-236; e) J. Ashok, M.L. Ang, P.Z.L.Terence, S. Kaw ChemCatChem, **2016**, *8*, 1308-1318, f) Z. Bian, S. Kawi, ChemCatChem, **2018**, *10*, 320-328; g) J. W. Geus, *Stud. Surf. Sci. Catal.* **1983**, *16*, 1-33; h) C. J. G. Van der Grift, A. Mulder, J.W. Geus, *Appl. Catal.* **1990**, *60*, 181-192; i) P. Burattin, M. Che, C. Louis, *J. Phys. Chem. B* **1998**, *102*, 2722-2732.

[6] P. Burattin, M. Che, C. Louis, *J. Phys. Chem. B* **1997**, *101*, 7060-7074; b) T. Lehman, T. Wolff, C. Hamel, P. Veit, B. Garke, A. Seidel-Morgenstern, *Microp. Mesop. Mater.* **2012**, *151*, 113-125.

[7] a) C. J. G. Van Der Grift, A. F. H. Wielers, B. P. J. Joghi, J. Van Beijnum, M. De Boer, M. Versluijs-Helder, J. W. Geus, *J. Catal.* **1991**, *131*, 178-189; b) Z. Huang, F. Cui, J. Xue, J. Zuo, J. Chen, C. Xia, *Catal. Today* **2012**, *183*, 42-51; c) L.F. Chen, P.J. Guo, M. H. Qiao, S.R. Yan, H.X. Li, W. Shen, H. Xua, K. N. Fan, *J. Catal.* **2008**, *257*, 172-180; d) T. Vrålstad, H.K. Magnusson, J. Sjöblom, *Microp. Mesop. Mater.* **2007**, *106*, 155-161; e) A. Loaiza-Gil, J. Arenas, M. Villarroel, F. Imbert, H. del Castillo, B. Fontal, *J. Mol. Catal. A: Chem.* **2005**, *228*, 339-344.

[8] J. C. Park, H. J. Lee, J. U. Bang, K. H. Park, H. Song, *Chem. Commun.* **2009**, 7345-7347.

[9] M. V. Sivaiah, S. Petit, J. Barrault, C. Batiot-Dupeyrat, S. Valange, *Catal. Today* **2010**, *157*, 397-403.

[10] M. V. Sivaiah, S. Petit, M. F. Beaufort, D. Eyidi, J. Barrault, C. Batiot-Dupeyrat, S. Valange, *Microp. Mesop. Mater.* **2011**, *140*, 69-80.

[11] G. J. de A. A. Soler-Illia, E. L. Crepaldi, D. Grosso, C. Sanchez, *Curr. Opin. Colloid Interface Sci.* **2003**, *8*, 109-126.

[12] C. Ciotonea, B. Dragoi, A. Ungureanu, A. Chirieac, S. Petit, S. Royer, E. Dumitriu, *Chem. Commun.* **2013**, *49*, 7665-7667.

[13] Z. Bian, S. Kawi, *Catal. Today* **2020***, 339*, 3-23.

[14] D. Y. Zhao, J. L. Feng, Q. S. Huo, N. Melosh, G. H. Fredrickson, B. F. Chmelka, G. D. Stucky, *Science* **1998**, *279*, 548-552.

[15] H. Liu, H. Wang, J. Shen, Y. Sun, Z. Liu, *Appl. Catal. A-Gen.* **2008**, *337*,138-147.

[16] T. Wang, C. Liu, X. Ma, W. Zhu, X. Lv, H. Zhang, *Nanomaterials* **2019**, *9*, 998-1010.

[17] P. Burattin, M. Che, C. Louis, *J Phys. Chem. B* **1999**, *103*, 6171-6178.

[18] Z. Bian, S. Kawi, *J.CO₂ Util.* **2017**, *18*, 345-352.

[19] J. C. Park, H. J. Lee, J. U. Bang, K. H. Park, H. Song, *Chem. Commun.* **2009**, 7345–7347.

[20] P. Gallezot, D. Richard, *Catal. Rev. Sci. Eng.* **1998**, *40*, 81-126.

[21]   A. R. Shashikala, A. K. Sharma, D. R. Bhandari, *Sol. Energ. Mat. Sol. C* **2007**, *91*, 629–635.

[22]   a) Ni: P. Ryabchuk, A. Agapova, C. Kreyenschulte, H. Lund, H. Junge, K. Junge, M. Beller, *Chem. Commun.* **2019**, *55*, 4969-4972; b) Co: Z. Wei, Y. Chen, J. Wang, D. Su, M. Tang, S. Mao, Y. Wang, *ACS Catal.* **2016**, *6*, 5816−5822; c) Co: F. Chen, A.-E. Surkus, L. He, M.-M. Pohl, J. Radnik, C. Topf, K. Junge, M. Beller, *J. Am. Chem. Soc.* **2015**, *137*, 11718−11724; d) Ni: V. Ayala, A. Corma, M. Iglesias, J. A. Rincon, F. Sanchez, *J. Catal.* **2004**, *224*, 170-177.

[23]   Co/Ni alloys: a) R. Yun, L. Hong, W. Ma, S. Wang, B. Zheng, *ACS Appl. Nano Mater.* **2019**, *2*, 6763−6768; b) L.J. Malobela, J. Heveling, W.G. Augustyn, L.M. Cele, *Ind. Eng. Chem. Res.* **2014**, *53*, 13910−13919; c) J. W. Zhang, D. D. Li, G. P. Lu, T. Deng, C. Cai, *ChemCatChem* **2018**, *10*, 4966-4972; d) B. Liu, F. Yuan, K. Jin, Y. Zhang, W. J. Weber, *J. Phys. Condens. Matter* **2015**, *27*, 435006-435013.

[24]   a) I. Dobrosz-Góómez, I. Kocemba, J. M. Rynkowski, *Appl.Catal. B* **2008**, 83, 240-255; b) Y. Li, L. Wang, R. Yan, J. Han, S. Zhang, *Catal. Sci. Technol.* **2015**, 5, 3682-3692; c) J. Cheng, P. Hu, P. Ellis, S. French, G. Kelly, C. M. Lok, C. Martin, *J. Phys. Chem. C* **2010**, *114*, 1085-1093; d) S. S. Kale, J. M. Asensio, M. Estrader, M. Werner, A. Bordet, D. Yi, J. Marbaix, P. F. Fazzini, K. Soulantica, B. Chaudret, *Catal. Sci. Technol.* **2019**, *9*, 2601-2607.

[25]   a) D. S. Wang, J. Tang, Y. G. Zhou, M. W. Chen, C. B. Yu, Y. Duana, G. F. Jiang, *Chem. Sci.* **2011**, *2*, 803-806; b) Y. Duan, L. Li, M. W. Chen, C. B. Yu, H. J. Fan, Y. G. Zhou, *J. Am. Chem. Soc.* **2014**, *136*, 7688-7700.

[26]   a) M.G. Prakasha, R. Mahalakshmy, K. R. Krishnamurthy, B. Viswanathan, *Catal. Today*, **2016**, *263*, 105-111; b) Y. Chen, J. Chen, *Appl.Surf. Sci.* **2016,** *387,* 16-27.

[27]   a) J. Wang, J. Liu, N. Yang, S. Huang, Y. Sun, Y. Zhu, *Nanoscale* **2016**, *8*, 3949-3953; b) A. Li, K. Shen, J. Chen, Z. Li, Y. Li, *Chem. Engineer. Sci.* **2017**, *166*, 66-76; c) B. Li, H. C. Zeng, *ACS Appl. Mat. Interfaces,* **2018**, *10*, 29435-29447; d) H. Wang, X. Li, X. Lan, T. Wang, *ACS Catalysis,* **2018**, *8*, 2121-2128.

FULL PAPER

FULL PAPER

Silica supported Bimetallic Nickel/Cobalt nanoparticles are produced from phyllosilicates reduction obtained by deposition precipitation over SBA-15. The catalysts were applied to the hydrogenation of imines, oximes and N-heretoarenes, displaying high activities and selectivities.

Carmen Ciotonea,* Nisrine Hammi, Jérémy Dhainaut, Maya Marinova, Adrian Ungureanu, Abdelkrim El Kadib, Christophe Michon and Sébastien Royer*

Page No. – Page No.

Phyllosilicate-derived Nickel-Cobalt bimetallic nanoparticles for the catalytic hydrogenation of imines, oximes and N-heteroarenes